Supporting Information for "Shear-convection interactions, and orientation of tropical squall lines"

Sophie Abramian[1], Caroline Muller[1], Camille Risi[1]

[1] Laboratoire de Météorologie Dynamique, IPSL, CNRS, Ecole Normale Supérieure, Sorbonne Université, PSL Research University, Paris, France

Contents of this file

1. **Model and simulations details.** In this section, we provide more detailed information on the cloud-resolving model used and the specific configurations of the simulations.

2. **Automatic detection of squall line angle: method description.** In this section, we describe in detail the method used in the paper to automatically detect the angle orientation of the squall line.

3. **Investigation of cold pool intensification with increasing background shear.** In this section, we analyze in more detail the changes of cold pool properties as the background wind is increased, and split this change into a change of cold pool depth and a change of cold pool averaged buoyancy anomaly.

4. **Investigation in cold pools, what are the origins of their intensification?**

In this section, we describe the average relative humidity and rain evaporation profiles above cold pools. This can help understanding the link between the cold pool height and the rain evaporation altitude.

1. Model and simulations details

We simulate several cases of squall lines using the Cloud-Resolving Model (CRM) System for Atmospheric Modeling, or SAM (Khairoutdinov & Randall, 2003). This model is based on a non-hydrostatic and anelastic formulation of atmospheric flows. It has the ability to cover a wide range of scales, from deep convective kilometric scale to mesoscale organization $\mathcal{O}$(100s km), and is thus adapted to the study of mesoscale systems such as squall lines. The prognostic thermodynamic variables of the model include total non-precipitating water (vapor, cloud water, cloud ice) and total precipitating water (rain, snow, graupel). The mixing ratios of cloud water, cloud ice, rain, graupel, and snow is diagnosed from the prognostic variables using a temperature-dependent partition between liquid and ice phases. The frozen moist static energy, which is the sum of the liquid/ice water static energy and the total condensate amount times the latent heat of vaporization, is conserved during moist adiabatic processes in the model, including the freezing and melting of precipitation. The model is run to radiative-convective equilibrium, and once equilibrium is reached (in about 30 days) the organization of squall lines is analyzed, from day 30 to 35 with hourly outputs.

All simulations are three-dimensional on a square, doubly periodic horizontal domain, with horizontal resolution 1 km and domain size 128 km in x and y directions. The vertical grid has 64 levels (capped at 27 km with a rigid lid), with the first level at 37.5 m and grid spacing gradually increasing from 80 m near the surface to 400 m above 6 km, and a variable time step (10 s or less to satisfy the Courant–Friedrichs–Lewy condition). The surface fluxes are computed using Monin–Obukhov similarity. To reduce gravity wave

reflection and buildup, a sponge layer with Newtonian damping is applied to all prognostic variables in the upper third of the model domain, from 18 to 27 km. We neglect the Earth rotation, a reasonable assumption in the deep tropics where the Coriolis parameter is small (set to zero in our simulations).

To organize the deep convection into squall lines, a linear shear in the x direction is imposed (following Muller (2013)). The imposed profile has a wind in the x-direction decreasing from U_{sfc} at the surface $z = 0$ km to $U_{1km} = 0$ m s^{-1} at $z = 1$ km. This background shear is imposed by relaxing the mean wind towards this profile with a relatively fast time scale of 2 hours. Nine simulations, with the surface wind U_{sfc} varied from 0 (no shear) to 20 m s^{-1}, with 2.5 m s^{-1} increments, are performed. To avoid an impact of this imposed surface wind on surface latent and sensible fluxes (which are proportional to surface wind magnitude), the domain-mean surface wind is removed before computing those surface fluxes.

2. Automatic detection of squall line angle: method description

Figure 2 bottom panels in the paper shows the autocorrelation of the precipitable water at convective radiative equilibrium, for the sub-optimal $U_{sfc} = 2.5$ m s^{-1}, near-optimal $U_{sfc} = 10$ m s^{-1}, and super-optimal $U_{sfc} = 17.5$ m s^{-1} cases. In the sub-optimal case, we have the characteristic signal of a white noise, random, since we observe a peak in the center and a fast diffusion of the signal. In the optimal case, the orientation is along the y axis, consistent with the PW spatial distribution (top panels). In the super-critical case, a similar pattern is observed, with the two axes oriented at an angle. Thus the

autocorrelation fields yield a centered representation of the convective organization. This next step will allow an automatic post-processing to measure the angle of the squall lines.

The angle a is defined as the angle between the squall line and the y-axis. To compute it, at each time step, we calculate the product between the spatial autocorrelation of PW (bottom contour plots of figure 2 in the main text) and a long (lengths 1 and 0.1 for major and minor axes) rotating 2D Gaussian oriented by a varying angle a. The selected angle a is the one that maximizes this product, i.e. that accounts for the best correlation.

By applying this method to all snaphots, we obtain a time distribution of the angle of the squall line with respect to the y-axis (between -$\pi/2$ and $\pi/2$). The mean of this distribution of angles in absolute value (between 0 and $\pi/2$) is our final angle, and its variance the incertitude (bottom curve in figure 2 of the main text).

Figure S1 shows the time evolution of the angle distribution for the three aforementioned cases. On the ordinate, we have the angle which varies from $-\pi/2$ to $\pi/2$, and on the abscissa, the time from the RCE equilibrium to the end of the simulation (5 days). Each pixel represents the probability density of an angle at a given time. In white, the evolution in time of the most probable angle is plotted. In the control case, we notice that the distributions are very wide, and decorrelated from one instant of time to another. In the sub-critical case, we have peaks around 0 during the whole evolution. In the super-critical case, we have three periods, first peaks of probability at -50, then a transition phase, and finally peaks in +50. This accounts for the indistinguishability between the 'right of the pool' and the 'left of the pool' for the projection of the angle, which sometimes gives rise to a broken line, similar to a V-shape.

From the time evolution of the angle distributions for each simulation, we can determine an averaged angle. We first reduced the angle to values between $[0, \pi/2]$ by taking its absolute value. Therefore, the final angle selected by our automatic method is the average over time of the absolute value of the most probable angle. We associate to each angle a measurement uncertainty, which corresponds to the variance of the distribution of the most probable angle (again in absolute value) in time. This method yields the angle estimate versus shear strength shown figure 2 bottom panel of the main paper. We note that this method has been tested on several data sets and compared to repeated and rigorous manual measurements, which attests to the reliability of this approach.

3. Investigation of cold pool intensification with increasing background shear

Here we investigate whether the cold pool intensification with shear strength is due to the increase in depth, or to the increase in the buoyancy anomaly. We therefore calculate the contribution to changes in cold pool potential energy E_p from the height of the cold pool h and from the mean buoyancy anomaly in the cold pool E_p/h. To do this, we develop the energy as follows:

$$\frac{\Delta E_p}{E_p} = \frac{\Delta(E_p/h)}{(E_p/h)} + \frac{\Delta h}{h} + \mathcal{O}(\Delta^2) \tag{1}$$

where Δ is defined as

$$\Delta\phi = \frac{\phi_{ctrl} - \phi}{\phi_{ctrl}} \tag{2}$$

and Δ^2 denotes a second order error term (involving $\Delta(E_p/h) \times \Delta(h)$).

Figure S2 shows for each case this decomposition of the potential energy change. For example, for the case $U_{sfc} = 20$ m s^{-1}, we see that the potential energy has doubled compared to the control case; it has increased by 20% compared to the optimal case. This figure shows that the evolution of the potential energy is mainly due to the increase of the height, with a smaller (but not negligible) contribution from increased buoyancy anomaly. We interpret these changes as resulting from the drier conditions, yielding higher and larger rain evaporation with increasing shear, as further discussed in the main text.

4. Investigation in cold pools, what are the origins of their intensification?

In the graph S3 the vertical profiles of the relative humidity in dashed line, as well as the rain evaporation rate (QPEVP) in solid lines are displayed for each cases. The relative humidity field is calculated following Clausius-Clapeyron approximation. The rain evaporation rate is an output of the cloud resolving model SAM. We compute both these quantities in a composite way, i.e. we average in the vicinity of maximum precipitation at each time step. The vertical profiles are obtained by averaging in x and y near the maximum of precipitation (10km in x, 5km in y). In this graph, the thresholds QPEVP=34 g/kg/day and RH=0.9 are highlighted too.

Considering the relative humidity profiles (dashed lines), we observe that as the shear increases, the dry layers is deeper. In fact, at z=400m, the relative humitidy is equal to 0.875 for the control case, whereas it is equal to 0.825 for the highest shear case. In the meantime, we observe that for the higher shear cases, the increase of the evaporated rain fraction, namely the rain evaporation process, occurs at higher altitude. For example, at

z=1000m, the rain evaporation is equal to 25g/kg/day for the control case U=2.5m/s, and reaches 34g/kg/day for the case U=20m/s.

To summarize, as the shear increases, the rain evaporation occurs at higher altitude, which deepens the dry layer and this leads to the expansion in height of the cold pools.

References

Khairoutdinov, M. F., & Randall, D. A. (2003). Cloud resolving modeling of the arm summer 1997 iop: Model formulation, results, uncertainties, and sensitivities. *J. Atmos. Sci.*, *60*(4), 607-625.

Muller, C. J. (2013). Impact of convective organization on the response of tropical precipitation extremes to warming. *J. Climate*, *26*, 5028–5043.

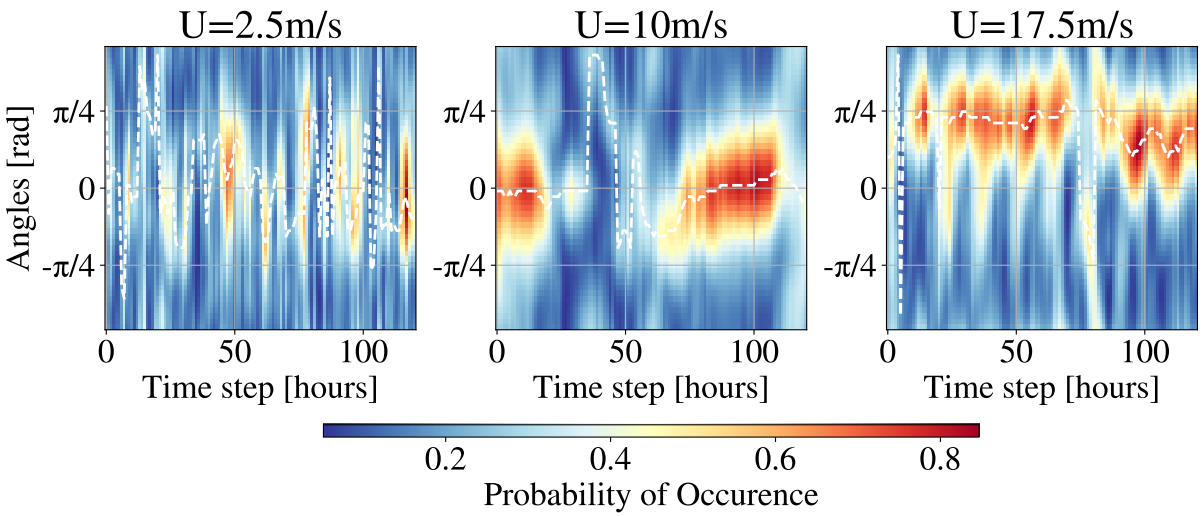

Figure S1. Time evolution of the distribution of angles of the squall lines with respect to the y-axis (perpendicular to the incoming wind) determined from the PW autocorrelation images.

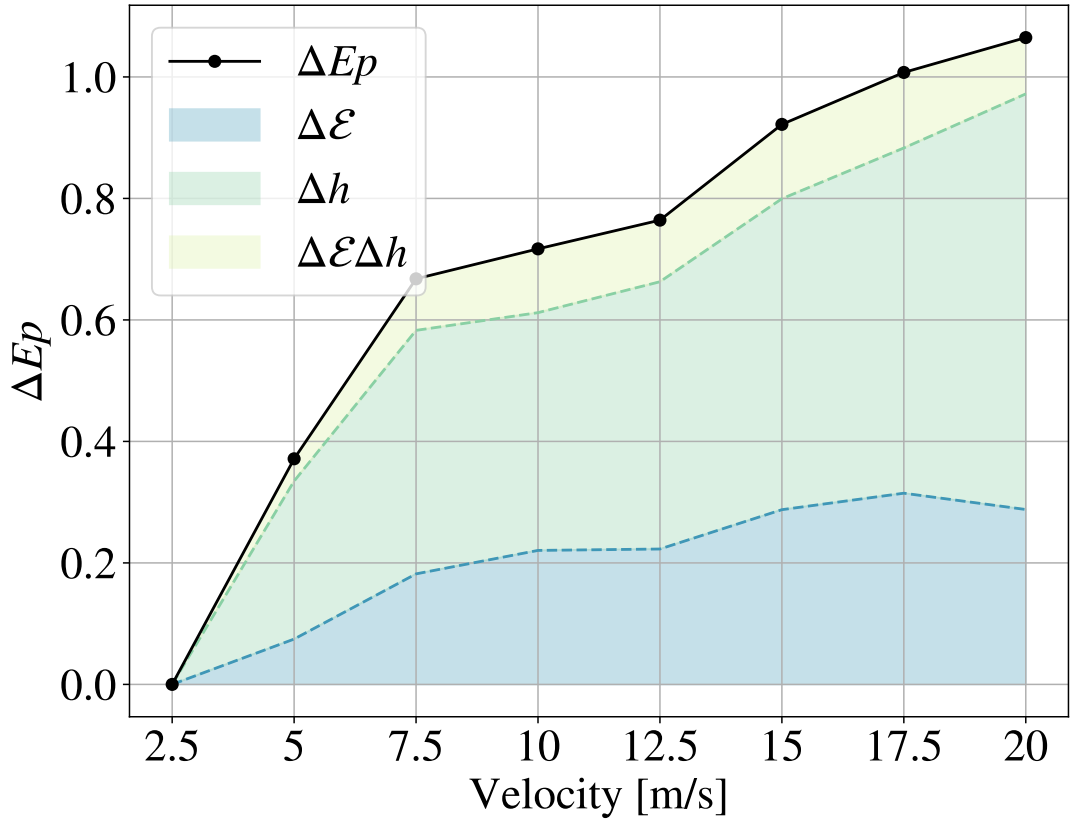

Figure S2. Evolution of the differential of the potential energy as a function of the shear strength. The differential is defined as $\Delta Ep = (Ep - Ep_{ctrl})/Ep_{ctrl}$. For each simulation, ΔEp is decomposed into a contribution from cold pool height and cold pool strength (and the second order error term). This figure shows that the intensification of the cold pools is mainly the consequence of deeper cold pools with increasing shear.

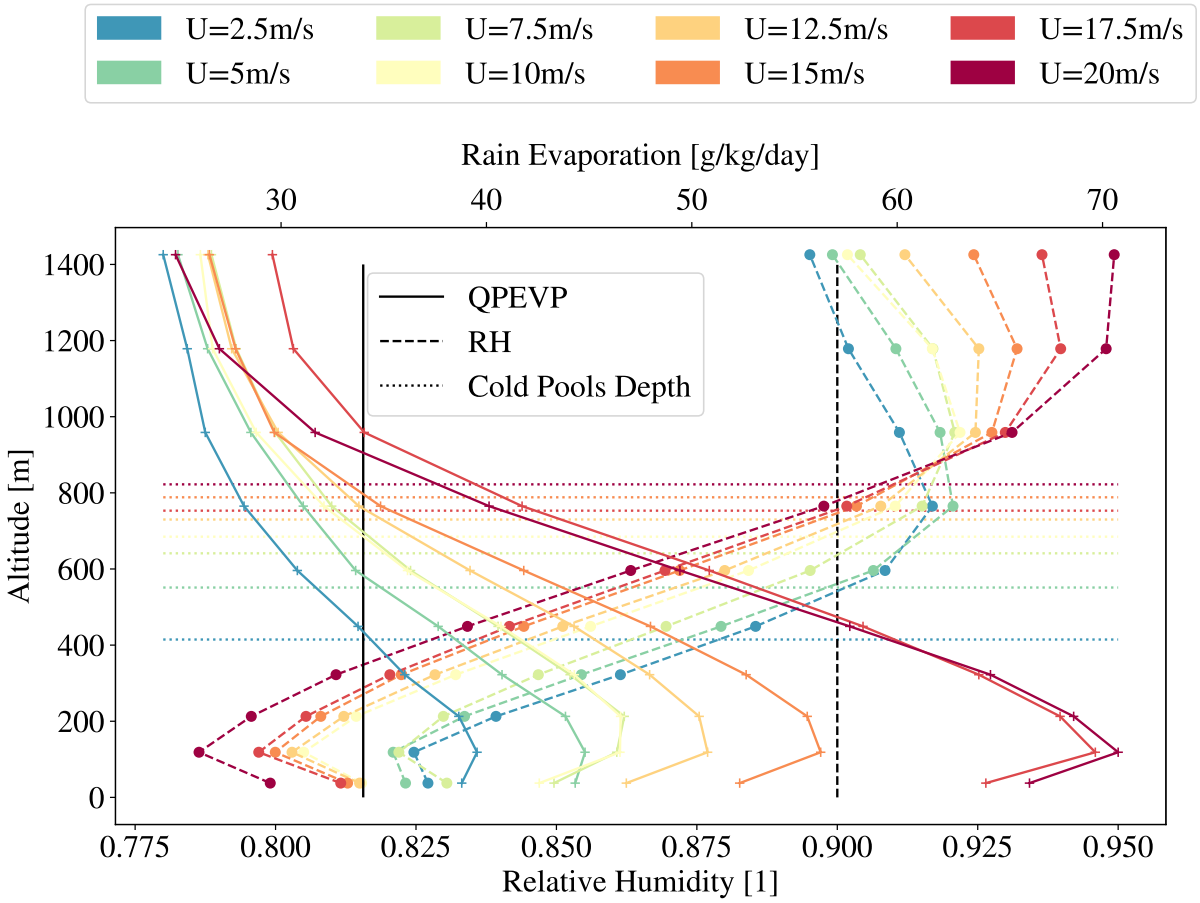

Figure S3. Vertical profiles of the relative humidity (dashed lines) and rain evaporation rate (solid lines). Cold pools depths are displayed in dotted lines. Each color represents a shear case. The threshold QPEVP=34g/kg/day and RH=0.9 are highlighted.